RSC Advances

PAPER

View Article Online
View Journal | View Issue

Cite this: *RSC Adv.*, 2017, 7, 11478

Smart and designable graphene–SiO_2 nanocomposites with multifunctional applications in silicone elastomers and polyaniline supercapacitors

Hualan Wang,*[a] Risheng Liu,[a] Cheng Yang,[a] Qingli Hao,[b] Xin Wang,[b] Kai Gong,*[c] Jirong Wu,*[a] Yingqian Hu,[a] Zhifang Li[a] and Jianxiong Jiang[a]

Received 7th January 2017
Accepted 1st February 2017

DOI: 10.1039/c7ra00262a

rsc.li/rsc-advances

A novel method was developed to promote the multifunctional applications of chemically reduced graphene (rGE) in silicone elastomers (SE) and polyaniline (PANI)-based supercapacitors *via* the integration of SiO_2. With the help of SiO_2, the surface status of rGE can be designed according to actual needs and the generated rGE–SiO_2 (rGES) showed various microstructures including lamellar, dendritic and sandwich-like shapes. The microstructures of rGES played a decisive role in the final functions of rGES-based polymer nanocomposites, which were better than the rGE-based polymer matrixes. Generally, lamellar rGES retained and stimulated the advantages of rGE, and the rGES-integrated PANI electrode (rGESP) showed better specific capacitance (555 F g^{-1}) and cycling life (91%) than the rGE-integrated PANI electrode (381 F g^{-1} and 79%). Sandwich-like rGES promoted the mechanical performances of SE, and the values of rGES/SE (rGESSE) are ten times higher than those of rGE/SE, from 0.4 MPa to more than 7 MPa for the tensile strength and from 0.28 MPa to 3.7 MPa for the tensile modulus. Thus, the fabricated rGES is smart and designable, displaying multiple functions and applications.

1. Introduction

Multifunctional materials[1–3] have attracted significant interest due to their diverse functions and flexibility, which are more adaptable than single functional materials. Graphene has further developed this type of materials due to unique properties such as high electrical conductivity, large specific surface area, excellent mechanical properties, high thermal conductivity and ease of functionalization.[4–7] Graphene can not only show a variety of functions effectively in a single form,[8–11] but can also serve many purposes in different fields of applications.[12–15] For instance, Youngblood[16] demonstrated a single graphene-based device that simultaneously provided efficient photodetection and optical modulation. Yan[17] reported multifunctional three-dimensional graphene foams for high-performance supercapacitors and absorbers of hazardous organic liquids. Hence, graphene is able to achieve versatility individually.[18,19]

There are also some multifunctional examples of graphene derivatives[20,21] or graphene hybrids with other forms of carbon.[22] For example, Wang[23] combined graphene sheets and nanoribbons to form ultra-low density, highly porous, compressible and elastic aerogels for supercapacitor electrodes and adsorbents. Ye[24] constructed graphene-tethered carbon fiber composite paper that was suitable as an electrocatalyst for oxygen reduction, oxygen evolution and hydrogen evolution reactions.

The versatility of graphene can also be displayed in the form of composites with polymers. Graphene can usually be directly introduced into the polymers.[25–29] Wu[30] used an alternating-current electric field to align graphene nanosheets in an epoxy polymer to simultaneously enhance mechanical, electrical, and thermal properties. However, graphene and polymers sometimes suffer from the limitations of poor compatibility, and functionalization of graphene is an effective choice to obtain the desired results. For example, Xue[31] synthesized POSS-functionalized graphene nanosheets that showed superhydrophobic properties and could be used as nanofillers to increase the decomposition temperature and glass transition temperature for polymers. Yang[32] incorporated polydopamine-coated graphene into polyurethane to enhance the tensile, thermomechanical, electromagnetic interference shielding properties and to reduce the electrical conductivity percolation threshold of the nanocomposites. Mai[33] fabricated a polymethylmethacrylate (PMMA)

---

[a] *Key Laboratory of Organosilicon Chemistry and Material Technology, Ministry of Education, Hangzhou Normal University, No. 58, Haishu Rd, Hangzhou, 311121, China. E-mail: hualanwang@163.com; 23wjr@163.com*

[b] *Key Laboratory of Soft Chemistry and Functional Materials, Ministry of Education, Nanjing University of Science and Technology, No. 200, Xiao Lingwei Street, Nanjing, 210094, China*

[c] *School of Pharmaceutical Science, Jiangnan University, No. 1800, Lihu Avenue, Wuxi, 214122, China. E-mail: kingong222@163.com*

matrix by introducing imidazolium ionic liquids to non-covalently functionalized graphene, which contributed to the large increases in the glass transition temperature and storage modulus.

Besides the above mentioned species, metals[34] or their oxides[35–37] are also able to expand and strengthen the multi-functions of graphene. Rajesh[38] synthesized nanohole-structured and palladium-embedded 3D porous graphene for ultrahigh hydrogen storage and CO oxidation multifunctions. Liu[39] presented nitrogen-rich carbon coupled multifunctional metal oxide/graphene nanohybrids for long-life lithium storage and efficient oxygen reduction. Upadhyay[40] reviewed that metal oxide/graphene composites can perform multiple roles including (but not limited to): photocatalysts, adsorbents, antimicrobial agents. Wang[41] prepared magnetic Fe_3O_4/graphene oxide nanocomposites with controlled drug delivery and magnetic resonance imaging.

However, there are still some unsettled issues about multi-functional graphene composites with metals, metal oxides and polymers. For example, many metals, especially transition metals and their oxides, are harmful to biology, and the destruction to the environment is irreversible. Moreover, some metals and their oxides are very precious with limited abundance on Earth. The excessive exploitation of resources may make them more expensive and rarer in the future. For another example, graphene is sometimes hard to bind and disperse in polymers, leading to inadequate performance release of graphene. Therefore, developing low cost, green, sustainable and well dispersed graphene based multifunctional materials has become a great challenge.

In this work, we have focused on exploring the potentials of SiO_2 in promoting the multiple applications of rGE in silicone elastomers (SE) and polyaniline (PANI) supercapacitors. Silicon (Si) and oxygen (O) are the most abundant two elements, constituting 26.4% and 49.4% of the total mass of the earth's crust, respectively. If nonmetallic SiO_2 could be utilized effectively, the resources and environmental advantages of SiO_2 would exceed most metals, metal oxides and transition metal oxides. Therefore, more attention should be concentrated on SiO_2, a low cost and environmental friendly material. And so far, it is still unknown whether such nonmetallic oxides can amplify and intensify the versatility of graphene or not. We expect to observe improvements in SiO_2 promoting and expanding the multiple functions of graphene in various areas.

2. Experimental section

2.1 Fabrication of rGES

Graphite oxide (GO) was prepared using graphite (500 mesh) according to other literature by the Hummers method.[42,43] Firstly, GO (5 g) in ethanol/distilled water (5000 mL, volume ratio 10 : 1) was ultrasonicated for 1 h in a KQ-600 ultrasonic cleaner (600 W, Kunshan Ultrasonic Instrument Co., Ltd., China) to get a partly exfoliated yellow brown graphene oxide (GEO) suspension. Secondly, the dispersion was transferred to a flask (10 000 mL), and a suitable amount of tetraethylorthosilicate (TEOS, CP.) and ammonia (AR.) were added into the solution under stirring. The mixture with a pH of 9–10 was reacted for 1 h at room temperature to prepared the GEO/SiO_2. Thirdly, the hydrazine hydrate (AR., 6.25 mL, 69 millimol) was added to the dispersion, and the temperature was increased to 75 °C with refluxing and stirring for 3 h to prepare the reduced graphene/SiO_2 (rGES). The fabricated rGES was collected, rinsed and dried in a vacuum at 80 °C. By changing the amount of raw materials, GO and tetraethylorthosilicate, a series of rGES with different SiO_2 ratios were prepared.

2.2 Fabrication of rGES based polymer nanocomposites

Preparation of rGES@methyl vinyl polysiloxane matrix. Firstly, methyl vinyl polysiloxane (100 g, M_w 610 000, vinyl content 0.16% mol), rGES (5, 10, 20, 30 g), hydroxyl silicone oil (10 wt% of the rGES weight) and zinc stearate (CP, 0.1 g) were mixed on a SK-160 double roll open plastomil (Shanghai wings rubber machinery Co., Ltd, China) 5 times. Secondly, the mixture was put into a 150 °C vacuum oven for 4 h and taken out to cool before anti-refining with 2,5-dimethyl-2,5-di(*tert*-butylperoxy)hexane (1 g) on the SK-160 double roll open plastomil. Thirdly, the sample was put into a 11.5 × 11.5 × 0.25 cm mold and vulcanized (10 min, 170 °C, 14.5 MPa) on a QLB-50 vulcanizing machine (Shanghai wings rubber machinery Co., Ltd, China). Lastly, the sample was transferred into a blast oven (200 °C, 4 h) for depth curing and cut into strips before mechanical tests.

Preparation of rGES/polyaniline (rGESP) nanocomposite. rGES was dispersed in glycol/distilled water mixed solvents (5000 mL, volume ratio 1 : 1) under ultrasonication for 1 h in a KQ-600 ultrasonic cleaner. Then, the mixture of aniline (9.9 mL, 100 millimol) and concentrated hydrochloric acid (9.0 mL, 100 millimol) was added into the suspension and stirred for 30 min. After that, ammonium persulfate (APS, 24.48 g) was added. The molar ratio of aniline, hydrochloric acid and APS was 1 : 1 : 1. The reaction was conducted at room temperature for 1 h, and the color of the mixture changed from black to dark green. Finally, the mixture was filtered and washed with distilled water several times, and dried at 60 °C in a vacuum oven for 24 h. The composite was called rGESP.

Preparation of rGESP electrodes. The single electrode was prepared by mixing 85 wt% active materials, 10 wt% acetylene black and 5 wt% polytetrafluoroethylene as a binder. The mixture was dissolved in distilled water to form a slurry, and after manual grinding, the slurry was pressed onto a stainless steel and dried at 60 °C in a vacuum oven for 12 h. To make a good contact, the steel was pressed under 10 MPa for 2 min and dried for another 24 h at 60 °C.

2.3 Characterizations

Material characterizations. Powder X-ray diffraction (XRD) analyses were carried out using a Thermo ARL X'TRA with Cu-Ka radiation (l = 1.5406 Å). Fourier transform infrared spectroscopy (FT-IR) was performed with a Nicolet 7000 using KBr pellets. Morphological analyses of samples were carried out on an H-7650 transmission electron microscope (TEM, Hitachi, Japan) and an SEMS-3000N scanning electron microscope (SEM, Hitachi, Japan).

Electrochemical tests. All electrochemical experiments were carried out in 1 M H_2SO_4 using a three-electrode system, in which the sample was used as the working electrode, platinum foils as the counter electrode, and a saturated calomel electrode (SCE) as the reference electrode. Cyclic voltammetry (CV) measurements were performed with a LK2005B workstation at a potential range of −0.1 to 0.6 V. EIS was recorded under the following conditions: AC voltage amplitude 20 mV, frequency range 1×10^4 to 1×10^{-2} Hz at 0.3 V. Galvanostatic charge–discharge (CD) measurements were performed from −0.1 to 0.6 V with a Land Battery workstation at room temperature.

Mechanical tests. Mechanical properties were recorded on a material testing machine (Gotech Testing Machines Co. LTD, China). Tensile strength data were collected referring to GB/T528-1998 standard.

3. Results and discussions

3.1 Morphology of rGES

TEM images of rGES with the SiO_2 mass ratios 10, 50 and 90 wt% are shown in Fig. 1a, b, d, e, g and h, respectively. It can be seen that rGES-10 wt% is a lamellar structure that consists of approximately 2D wrinkled rGE and loaded nanoscale SiO_2. The average diameter of loaded SiO_2 is estimated to be less than 5 nm, according to the inset of Fig. 1b(i). The lamellar structure of rGES is much like the cross section of dragon fruit, shown in Fig. 1c. It is interesting that the lamellar structure changes into a 3D dendritic architecture when the SiO_2 ratio increases to 50 wt%, shown in Fig. 1d and e. The special dendritic rGES is composed of a highly folded internal skeleton and densely outstretched zigzags on the edges. The size of zigzags is in the range of 100–200 nm in length and 10–30 nm in width according to the inset Fig. 1e(ii). The dendritic rGES in appearance is like a butterfly, as shown in Fig. 1f. The possible cause of the particular morphology will be discussed in detail shortly.

Fig. 1g and h show that rGES-90 wt% develops into sandwich-like sesame cake architecture (Fig. 1i) with rGE as the core sheet and SiO_2 as the external wrapping layers. It is the increased number of SiO_2 particles that gradually covered the exposed regions of the rGE sheets on both sides and finally formed the outer sandwich-like structure. Compared with the lamellar structured rGES, obvious changes can be seen for sandwich-like rGES. For example, there is almost no exposed area on rGE, the sheets become thicker, and the size of SiO_2 is larger (10–20 nm), which is shown in the inset (iii) of Fig. 1h. The bigger size is because of the sustained increase and growth

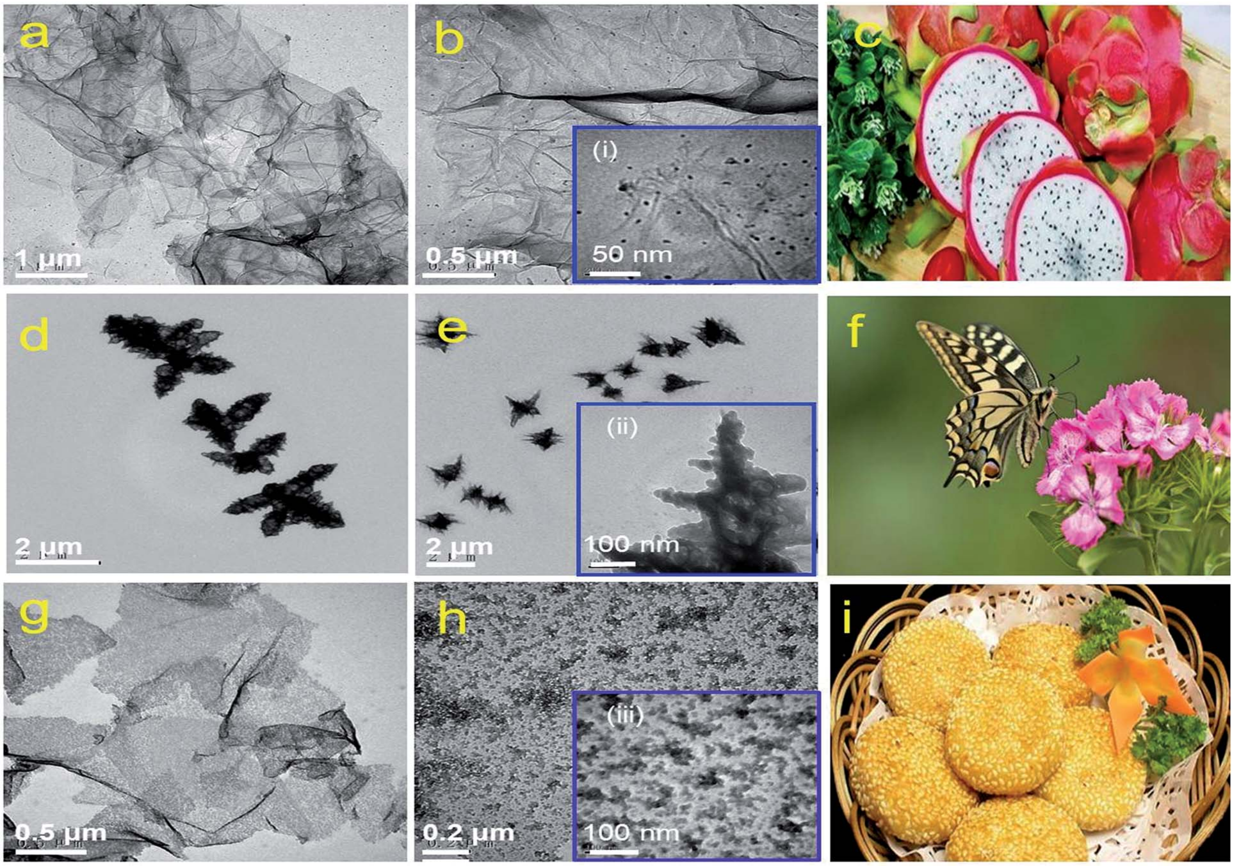

Fig. 1 TEM images of rGES with different SiO_2 mass ratios: (a and b) 10 wt% (d and e) 50 wt%, (g and h) 90 wt%. The insets (i, ii, iii) are higher magnifications of rGES-10 wt%, rGES-50 wt% and rGES-90 wt%, respectively. The color images (c), (f) and (i) are figures of speech for rGES-10 wt%, rGES-50 wt% and rGES-90 wt%, respectively.

of SiO_2. Thus, three kinds of typical morphology, 2D lamellar, 3D dendritic, and sandwich-like rGES have been regulated simply by controlling the relative amount of raw materials.

It has been suggested that when the mass ratio of SiO_2 is lower than rGE in rGES, SiO_2 acts as the object and rGE acts as the body to show loaded structures. Conversely, when the SiO_2 content exceeds rGE, SiO_2 and rGE act as the body and object, respectively, in rGES, showing a sandwich-like biscuit architecture. However, when the contents of the two are nearly equal, there is an intense competition to get the body identity between rGE and SiO_2. It is hard to determine the winner, and they finally act as a framework for each other. As a result, the rGE regions containing SiO_2 become the skeleton, which is quite thick due to the wrinkling and stacking in the competition process. The exposed rGE regions without SiO_2 become edges that are very thin and quite branched. Therefore, the 3D dendritic-like structure may be a result of competition, reflecting the intermediate or transition state between the lamellar state and sandwich-like structure.

Fig. 2a, d and g show the digital photos of the fluorescence screen for rGES-50 wt% taken from the observation window of the TEM instrument. These photos clearly display several artistic distributing states of rGES-50 wt% on the carbon support film of the copper mesh: apple, circle, and stars situated in a circle. Fig. 2b, e and h are the corresponding images of these samples collected by a TEM instrument equipped with a CCD camera at lower magnification. Whatever the accumulation mode is, the microcosmic morphologies are nearly the same. They are wrinkled and branched into a 3D hierarchical structure with sawtooth edges, as shown in Fig. 1d and e and 2c, f and i.

Detailed microstructural analysis of rGES-50 wt% by the TEM technique at the nanoscale reveals that these 3D hierarchical structures are formed in accordance with a certain way. The sawtooth edges are more likely from the discontinuous areas where rGE is not covered by SiO_2. Thus, one possible formation mechanism for this 3D dendritic structure is that the rGE regions containing the SiO_2 fold and stack in the center forming the skeleton, and the exposed rGE area without SiO_2 naturally stretches around forming the zigzag edges.

Based on the variable structures mentioned above, we believe that rGES has potential diverse functions when used in

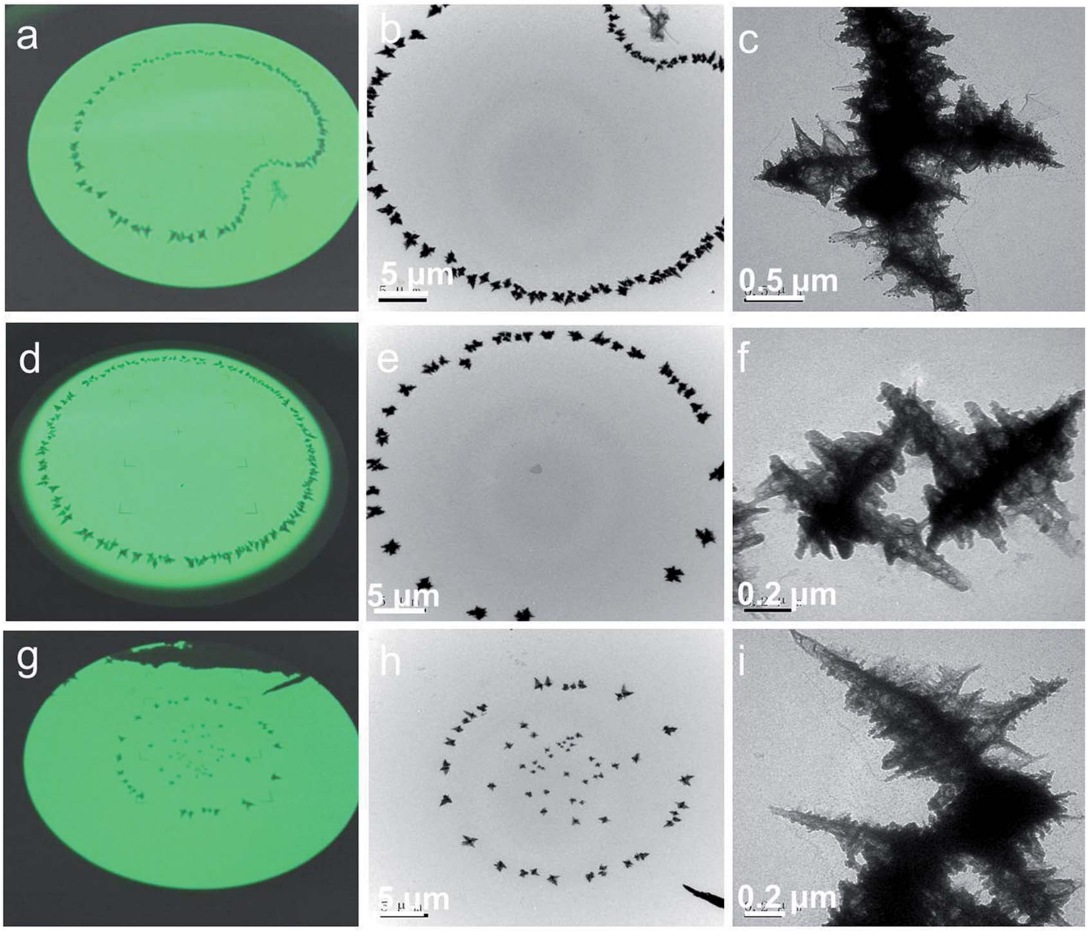

Fig. 2 rGES-50 wt% has several artistic distributing states on carbon support film of copper mesh: (a) apple, (d) circle, (g) stars situated in a circle. The first vertical column (a, d and g) is digital photos of the fluorescence screen shooting from the observation window of the TEM instrument. The second vertical column (b, e and h) TEM images of rGES-50 wt% recorded by the CCD camera of the TEM instrument at lower magnification. The third vertical column (c, f and i) corresponding TEM images recorded at higher magnifications, respectively.

polymers because the microstructure always determines the final performance of materials. One possible function is based on lamellar rGES, which may be a good electrode material for PANI based supercapacitors due to a large exposed area of rGE in rGES. The other possible function is based on sandwich-like rGES, which may act as enhancing filler for silicone matrixes due to the excellent compatibility between rGES (through SiO_2) and silicone. The 3D dendritic structure is proposed as a critical point of function conversion from electrochemical to mechanical properties. Therefore, rGESSE and rGESP matrixes are constructed and discussed systematically to verify the speculations experimentally. We investigated the mechanical enhancing effect of rGES on silicone matrixes.

3.2 The rGES as an enhancing filler for silicone elastomers

The relationship between the tensile strength of corresponding silicone matrixes and SiO_2 content in rGES is shown in Fig. 3. The tensile strength of pure rGE filled silicone matrix is about 0.4 MPa, corresponding to zero content of SiO_2 in rGES. Increasing the filling fraction of rGE does not improve the tensile strength value, indicating that the mechanical property of rGE has not been utilized sufficiently. Poor compatibility between rGE and silicone may be an important reason, leading to poor dispersion. When the ratio of silica in rGES is below 75 wt%, the tensile strength of the rGES filled silicone matrix is still low and almost constant, except for a small oscillation at 50 wt%. However, the tensile strength value increases rapidly as the silica ratio exceeds 75 wt%, which can be considered as a threshold. Afterwards, the tensile strength value rises quickly and exceeds 7 MPa for rGES-90 wt% at a filling fraction of 30 wt%, equivalent to a content of 3 wt% for rGE. The tensile strength value for the rGESSE matrix reaches more than 18 times the individual rGE filled one. The good compatibility of SiO_2 with silicone is helpful to aid the uniform dispersion of rGE in silicone, leading to better mechanical properties.

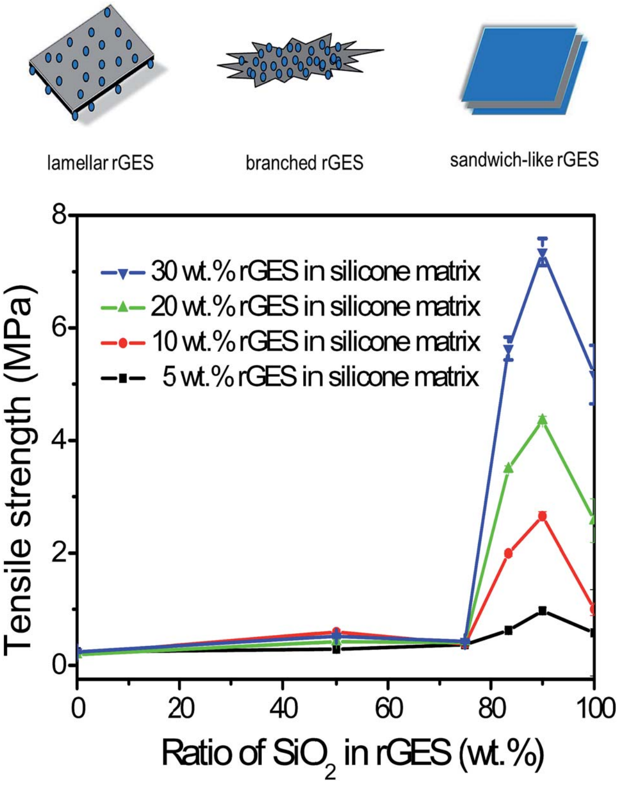

Fig. 3 Tensile strength as a function of SiO_2 content (0–100 wt%) in rGES. The filling fraction of rGES in the silicone matrix ranges from 5 wt% to 30 wt%. Here, rGES includes lamellar, branched and sandwich-like rGES.

It is observed that rGES with a higher ratio of SiO_2 at the threshold of 75 wt% has completely changed into sandwich-like structures (not shown here). That is to say, the function of mechanical enhancing is mainly realized by sandwich-like rGES. Here, the contact between rGE and silicone is achieved through SiO_2 indirectly. The incorporation of SiO_2 and its excellent compatibility with both rGE and silicone have improved the dispersion of rGE in the silicone matrix. Therefore, a higher ratio of SiO_2 in rGES leads to better dispersion in the silicone matrix and higher tensile strength. However, the tensile strength value declines when the silica content reaches 100 wt% (pure SiO_2), indicating that the components in rGES show synergy in the mechanical performance, exceeding both rGE and SiO_2. In addition, the tensile strength is also affected by the filling fraction of rGES, generally, a higher filling quantity leads to a bigger tensile strength value in our experimental ranging from 5 wt% to 30 wt%.

Young's modulus as a function of tensile strength is shown to further assess the mechanical performance of prepared silicone elastomers (SE) in Fig. 4. It was found that silicone matrixes filled by rGES with lower SiO_2 content (50 and 75 wt%) exhibit lower Young's modulus (<0.94 MPa) and tensile strength (<0.73 MPa). Only higher SiO_2 content in rGES (83 and 90 wt%) can bring significant improvement to Young's modulus (>3 MPa) and tensile strength (>5 MPa). In particular, the tensile modulus reaches 3.7 MPa at a rGES-90 wt% filling fraction of 30 wt%, nearly 5 times than the rGES-50 wt% filled one (0.8 MPa). From the TEM images in Fig. 1, we know that the higher SiO_2 content in rGES (>75 wt%) can greatly reduce the exposed specific area of rGE, which lacks compatibility with silicone. Conversely, SiO_2 possesses good compatibility with silicone chains; therefore, the interface contacts between silicone and rGES with higher SiO_2 ratios can be effectively improved. Compared with the reported graphene/silicone in literature,[44] the discussed rGESSE here shows better mechanical properties, implying a positive effect of the SiO_2 integration. The improved dispersion and properties allow wide applications of rGESSE as O-rings, high and low temperature sealed tubes, gaskets, button rollers and so on.

It seems that interfacial interactions directly influence the dispersion level of fillers in polymer matrixes. For each filled silicone nanocomposite, the microstructure for the cross-section of the tensile fracture was characterized by SEM. Fig. 5a–c shows the TEM images of sandwich-like rGES. Fig. 5d, e, f, g and h are the SEM images of silicone composites filled by rGE, SiO_2 and rGES, respectively. Fig. 5i is the SEM image of bare silicone for comparison. As for the rGE/silicone matrix,

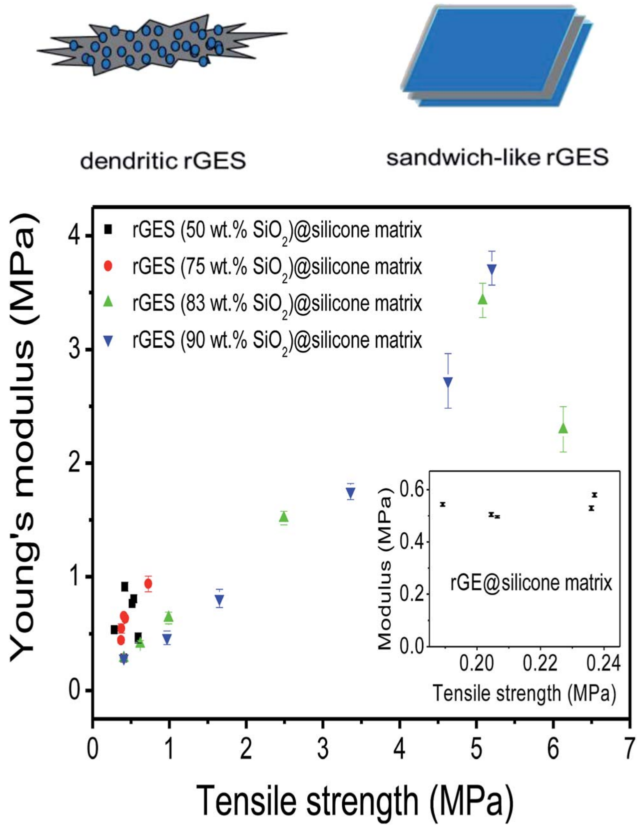

Fig. 4 The Young's modulus as a function of tensile strength. SiO$_2$ contents in rGES: 50, 75, 83, 90 wt%. The rGES filling fractions in silicone matrixes: 5, 10, 20, 30, 40 wt%. Here, rGES includes branched and sandwich-like rGES.

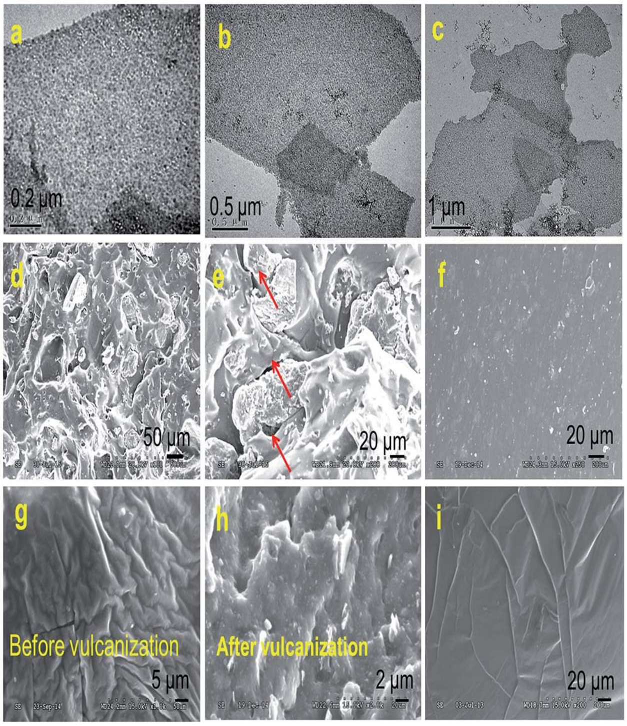

Fig. 5 (a–c) TEM images of sandwich-like rGES. SEM images of silicone matrixes filled by (d and e) rGE, (f) SiO$_2$ and (g and h) rGES, respectively. (i) Pure silicone.

obvious micro cracks (see the red arrows in Fig. 5e) were seen between the two phase interfaces, resulting from the extra force and weak interaction between the rGE and silicone. In particular, the appearance of the interphase micro crack under continuous external force was believed to be an important fuse leading to fracture behaviors. Compared with the situation of the rGE/silicone matrix, the fracture surfaces of SiO$_2$ and rGES filled silicone matrixes were more uniform and dense, and no obvious two phase interface micro cracks were observed. Furthermore, the dispersion states of rGES in the silicone matrix are far better than rGE and competitive to or even better than SiO$_2$.

Compared with the rGE/silicone, the SEM images of the silicone matrixes filled by rGES were more uniform. The vulcanized rGESSE matrix (Fig. 5h) shows a rougher surface than the one before vulcanization (Fig. 5g). The interactions between the rGES sheets and silicone are strong, and almost no micro-cracks emerge at the interfaces (Fig. 5h). On the other hand, however, the edges of the rGES sheets usually lack modification, especially for lower SiO$_2$ content samples. Therefore, the rGES edges are less compatible with silicone and are weaker positions where fractures are most likely to occur under external force. It was suggested that the fracture preferentially occurs at the weakest interaction positions. For example, the fracture for rGE filled silicone matrix preferentially occurs at the planar interface contacted with silicone. Conversely, the fracture for the rGES filled silicone matrix preferentially happens at the sheet edges in contact with silicone due to weaker compatibility. In addition to these, the fracture can also happen at crosslinking points and polymer molecular chains if the phase interfacial interaction is large enough under external force.

3.3 The rGES as active material for PANI supercapacitors

In order to further reveal the versatility of rGES in polymers, the rGESP nanocomposites were prepared to explore whether there is a positive effect of rGES on the PANI supercapacitors. The preparation was achieved by adding a certain amount of rGES in the formation process of PANI using an *in situ* polymerization method, the addition order of materials and manufacturing process is illustrated in Fig. 6a. Fig. 6b shows the XRD patterns of rGE, SiO$_2$, rGES, PANI and rGESP. The rGE shows a broad peak at 23.3°, signifying a certain degree of graphitization of rGE and corresponding to an interlayer spacing of about 0.38 nm. The peak of SiO$_2$ was found at 22.6°, which also emerges in the peak of rGES, whose peaks are a comprehensive reflection of rGE and SiO$_2$. A broad peak appearing at about 25° for PANI was observed, which is a typical polymer diffraction feature. After integrating with rGES in rGESP ternary composites, PANI shows several new peaks in the range of 15–40°, indicating that the regularity of PANI is enhanced largely. The existence of rGES promotes a more regular growth of PANI. Moreover, no obvious graphite peak at 26.6° can be found in

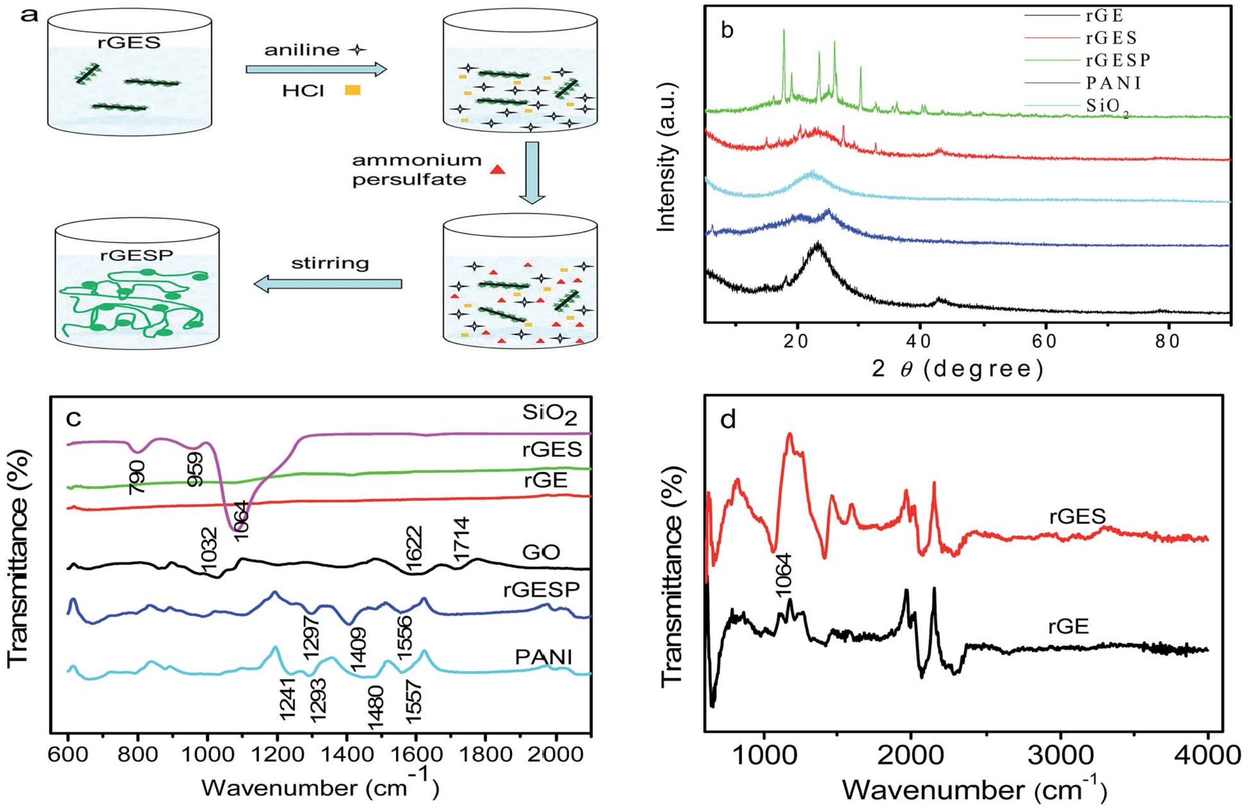

Fig. 6 (a) Fabrication route of rGESP. (b) XRD patterns of individual rGE, SiO_2, PANI and their nanocomposites rGES and rGESP. (c) FT-IR spectra of SiO_2, rGES, rGE, GO, rGESP and PANI. (d) Enlarged view for rGES and rGE in (c).

rGESP, indicating a good dispersion of rGE, and the agglomeration is inhibited by SiO_2 and PANI nanoparticles.

The FT-IR spectra of GO, rGE, rGES, rGESP, PANI and SiO_2 are compared in Fig. 6c. As we know, the characteristic peaks of GO at 1714 and 1032 cm^{-1} correspond to the carboxyl (COOH) and epoxide (C–O–C),[45] respectively. The peak at 1622 cm^{-1} can be attributed to the C=C stretching vibration.[46] Compared with GO, the rGE, rGES and rGESP show decreased or disappearing peak intensity for these oxygen-containing groups, indicating that GO was well reduced. For the case of SiO_2, the peak at about 790 cm^{-1} could be assigned to the typical vibration mode of the framework Si–O–Si; 1064 cm^{-1} is the asymmetric stretching vibration of Si–O–Si; and this peak also emerges in rGES just as shown in Fig. 6d. A weak band located at 950 cm^{-1} for SiO_2 was mainly attributed to the stretching vibrations of the Si–OH groups at defect sites.[47] For PANI, the peaks at 1557 and 1480 cm^{-1} correspond to the C=C stretching modes in quinoid and benzenoid ring for PANI, respectively. The peak at 1293 cm^{-1} was attributed to the C–N stretching vibration.[48] Most of the characteristic peaks of PANI and SiO_2 can be found in rGESP with a small chemical shift, indicating that the components are well combined and successfully constitute the final composite.

To understand and evaluate the role of SiO_2 on the capacitive character of an rGE based PANI electrode, it is necessary to figure out the role of SiO_2 on the corresponding electrochemical behaviors of rGES first. Fig. 7a gives the cyclic voltammetry (CV) of rGES electrodes with different SiO_2 mass ratios. The nearly rectangular CV curves of rGES demonstrate the electric double layer capacitor character,[49] covering all proportions of SiO_2 ranging from 5 wt% to 87.5 wt% at the scan rate of 10 mV s^{-1}. The CV curves of rGES-50 wt% at different scan rates from 1 to 100 mV s^{-1} (Fig. 7b) also indicate the efficient charge transfer and the nearly ideal capacitive behaviors. Although non-conductive and non-electrochemically active, SiO_2 is helpful to enhance the electrochemical response of rGE when added to less than 50 wt% (Fig. 7c) in rGES. However, it was observed that the specific capacitance of rGES decreased below the value of rGE when the amount of SiO_2 exceeds 50 wt% in rGES (Fig. 7d). That is because the conductivity of SiO_2 is poor, which is harmful to the whole electron transport of rGESP. Therefore, the role of SiO_2 on the capacitive character of rGES is adjustable and positive with suitable SiO_2 mass ratios (≤50 wt%).

The specific capacitance (C_s) from the CV can be calculated by using the formula[50] (1)

$$C_s = \frac{\int I\mathrm{d}V}{vmV} \tag{1}$$

where I is the response current, V is the potential window, v is the potential scan rate, and m is the mass of the electroactive materials. The detailed relationship between the specific capacitance of rGES and the SiO_2 ratio in rGES is summarized in Fig. 8a. The specific capacitance has the same changing trend at different scan rates, showing an optimum value at the SiO_2 ratio

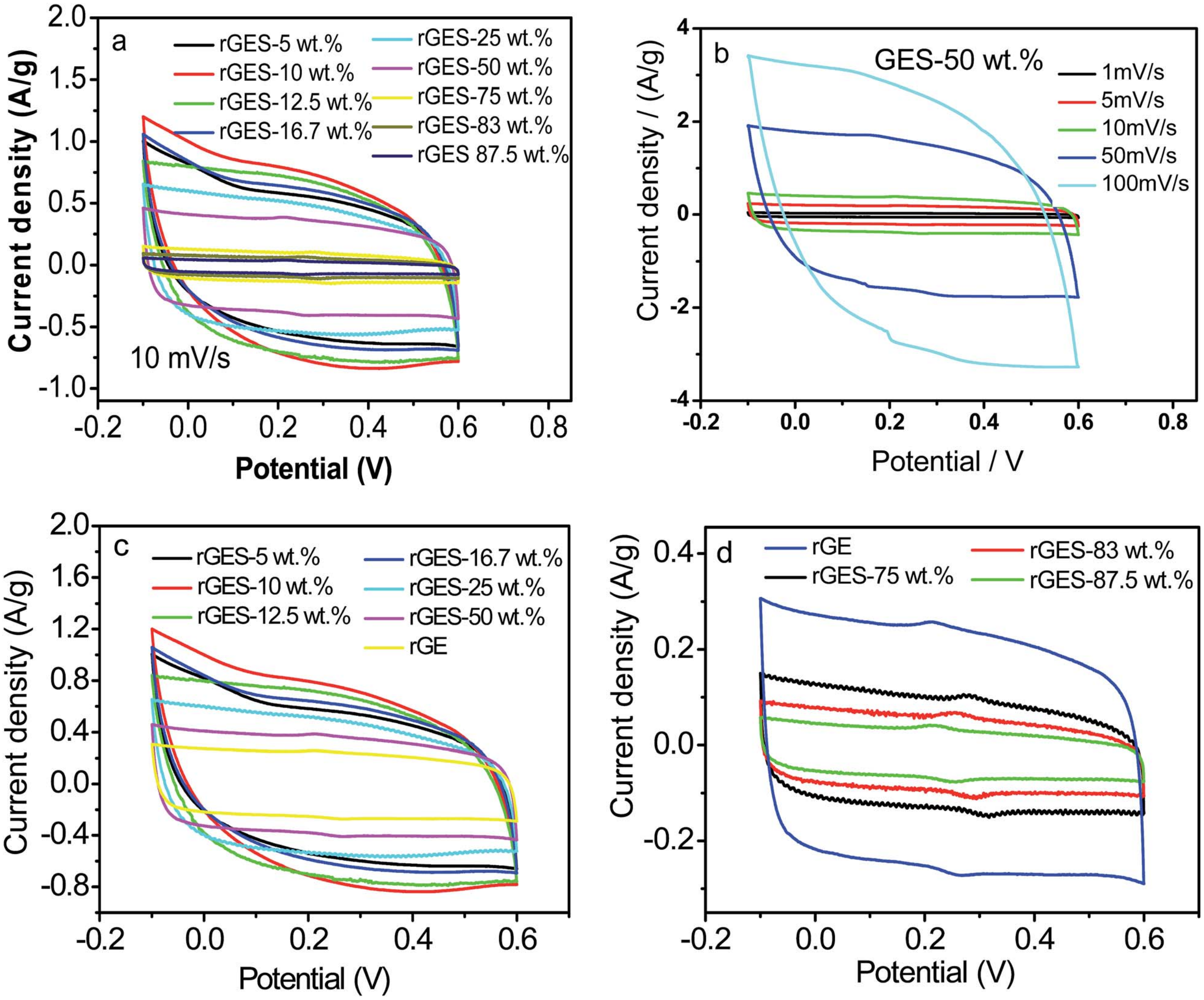

Fig. 7 (a) CV curves of rGES with different mass ratios of SiO_2 at the scan rate of 10 mV s^{-1}. (b) CV for GES-50 wt% at different scan rates ranging from 1 to 100 mV s^{-1}. (c) Enlarged view of (a) for rGES ≤ 50 wt% and rGE at a scan rates of 10 mV s^{-1}. (d) Enlarged view of (a) for rGES > 50 wt% and rGE at a scan rates of 10 mV s^{-1}.

of 10 wt%. Compared with 108 F g^{-1} of rGE at a scan rate of 1 mV s^{-1}, the specific capacitance value for rGES reaches 176 F g^{-1}. Although rGE shows wrinkled thin sheets with high theoretical specific surface area, it easily rebuilds together again because of van der Waals forces between the sheets in the solid state. Therefore, the increased capacitance value for rGES may result from the increased specific surface area utilization of rGE after integration of SiO_2 by overcoming the van der Waals forces and inter-layer stack.

Since rGES-10 wt% exhibits the best specific capacitance value among all the ratios, it was chosen and introduced into PANI instead of rGE to fabricate a series of rGESP hybrid materials. The mass ratio of rGES in rGESP in our experiments ranges from 0.56 wt% to 90.91 wt%. CV calculations indicated that the specific capacitance of the PANI electrode increases sharply after introducing a small amount of rGES (Fig. 8b). A peak C_s value of 555 F g^{-1} for rGESP was obtained at the rGES loading of 2 wt%, much higher than that of 381 F g^{-1} and 205 F g^{-1} for rGE/polyaniline (rGEP) and PANI at a scan rate of 1 mV s^{-1}. That is to say, a small amount of rGES addition is beneficial for the capacitance improvement for PANI, while 2–5 wt% are the best ratios, corresponding to a SiO_2 percent of 0.2–0.5 wt%. The improvements can be well maintained to different extents as the rGES ratio increases to a critical point at 50 wt%, and afterwards, the advantage disappears due to excess electrochemically inactive SiO_2.

The CV curves of rGE, rGES-10 wt%, rGEP and rGESP are compared and shown in Fig. 8c. A larger area of the closed CV loop is observed in rGESP, indicating the specific capacitance is higher than rGES, rGEP and rGE. A pair of redox peaks (the oxidation peak at about +0.2 V and the reduction peak at about +0.05 V) existed in rGEP and can also be found in rGESP at similar positions. The redox peaks of rGESP can be ascribed to a comprehensive effect of the changes in the PANI structures and the remaining oxygenated groups of rGE or in rGES. From the shape of the curves, we can see that rGESP retains not only

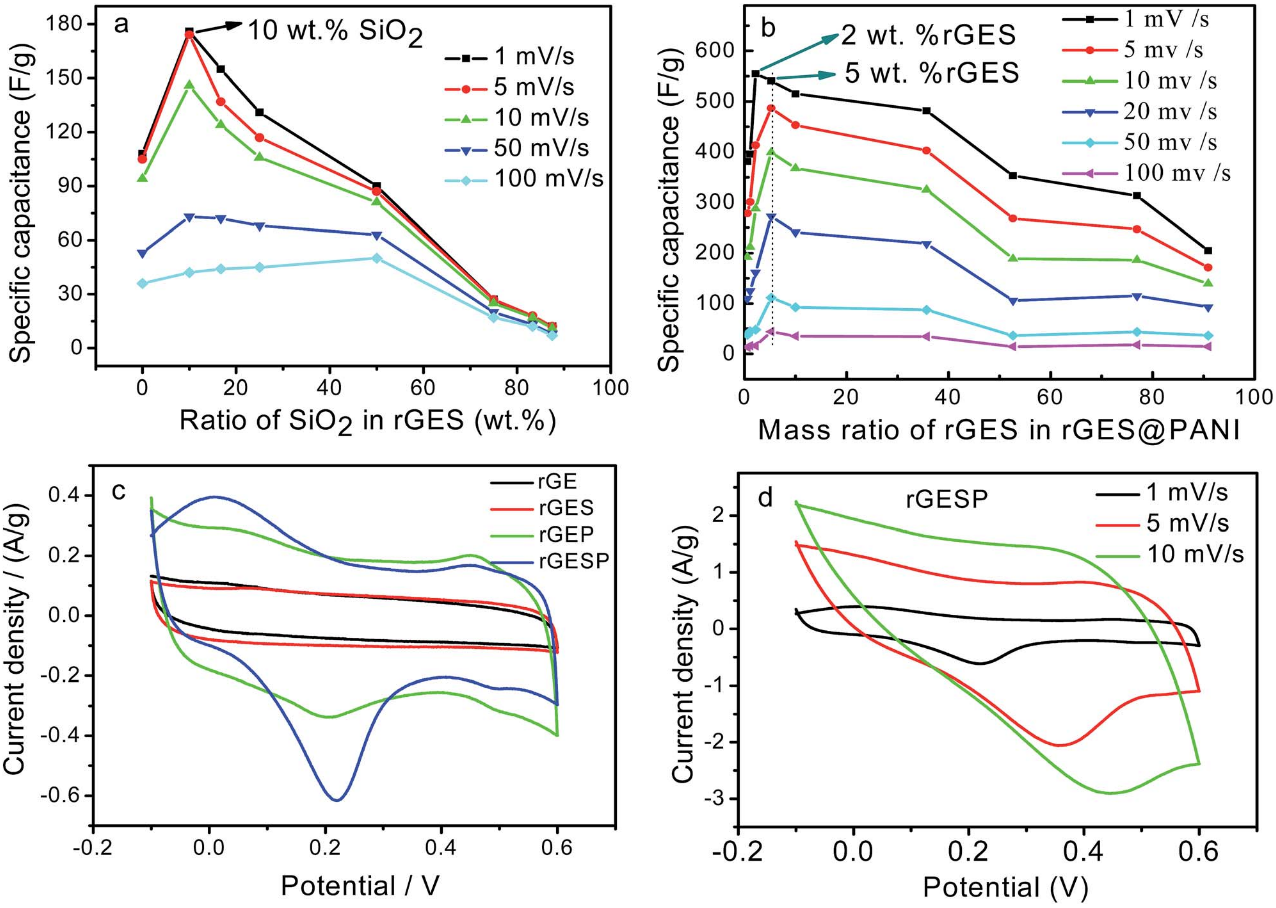

Fig. 8 (a) The specific capacitance of rGES as a function of the mass ratio of SiO_2 in rGES. (b) Specific capacitance of rGESP as a function of the rGES ratio in rGESP. (c) CV curves of rGE, rGES-10 wt%, rGEP, and rGESP at the scan rate of 1 mV s^{-1}. (d) CV curves of rGESP (with 2 wt% of rGES) at different scan rates 1–10 mV s^{-1}.

the EDLC of rGES but also the pseudocapacitance of PANI. Moreover, compared with rGEP, rGESP shows a larger area, indicating a better effect of rGES than rGE in improving the capacitance character of PANI supercapacitors. An obvious peak for rGESP with 2 wt% of rGES can be seen in Fig. 8d. The peak current density increases as the scan rate grows, and the shape of the CV curve does not change, exhibiting a good rate property.

To further understand the effect of rGES integration, the galvanostatic charge/discharge curves of rGES, PANI and rGESP were tested using a three-electrode system in 1 M H_2SO_4. As shown in Fig. 9a, the galvanostatic charge–discharge curve of PANI exhibits asymmetric triangular shapes, signifying the existence of pseudocapacitance and double layer capacitance in PANI. The observed pseudocapacitance originates from the oxidation–reduction of PANI chains. Compared with PANI, rGES-10 wt% shows a more symmetrical shape (Fig. 9b), implying a greater proportion of double layer capacitance and less proportion of pseudocapacitance. The relative symmetrical charge–discharge shape of rGES is consistent with its CV curves. In rGES, the residual oxygen groups of graphene provided pseudocapacitance while the carbon skeleton and SiO_2 provided double layer capacitance. The observed pseudocapacitance and double layer capacitance in PANI and rGES accordingly emerged in the curves of rGESP (Fig. 9c and d) at five different current densities. While a deviation from a symmetrical triangular shape was also observed in the curves of rGESP, revealing the combination of the EDL capacitance with faradaic capacitance, which is in agreement with the results obtained from the CV of rGESP in Fig. 8c and d.

As mentioned above, rGES exhibits a 2D lamellar structure when the SiO_2 ratio is lower than rGE. Interestingly, the lamellar rGES hides in the TEM images of rGESP and becomes difficult to identify as the ratio of rGES is very low (2 wt%). Instead, the observed TEM images are mainly attributed to PANI, the morphology of rGESP mainly shows the characters of PANI other than rGES (Fig. 10a and b). Two typical morphologies, spherical and fibrous PANI, can be seen as interconnected states in rGESP-2 wt%, which was prepared in ethanol/water mixed solvents. The two different morphology patterns are speculated and probably correspond to the two different solvent micro-environments: ethanol and water. Moreover, based on further observations, we believe that rGES possibly exists at the junctions between the spherical and fibrous PANI in the rGESP composites, as shown in the blue circle of Fig. 10b. This kind of connecting perhaps helps preventing or reducing the chance of

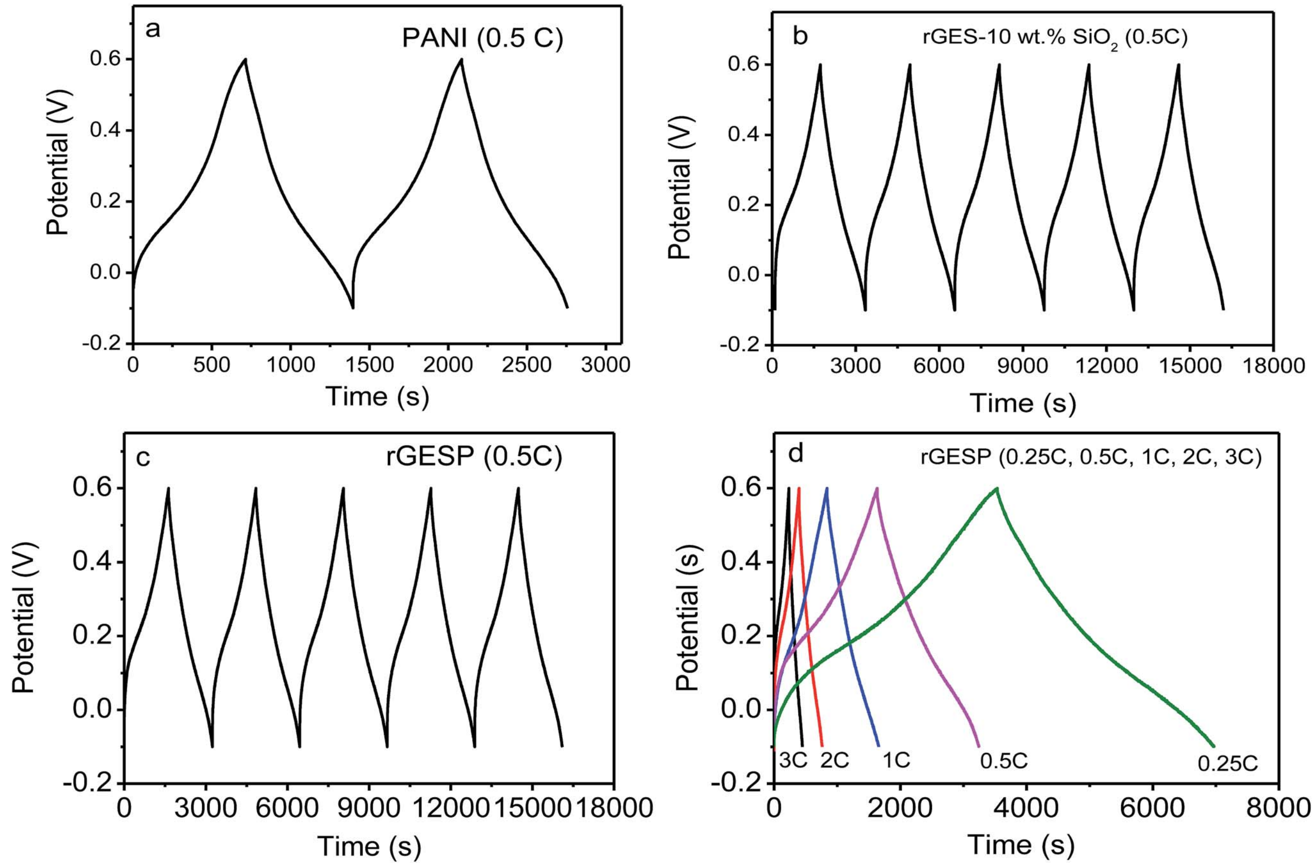

Fig. 9 Galvanostatic charge/discharge curves of (a) PANI, (b) rGES-10 wt% SiO_2, (c) rGESP at 0.1 A g^{-1} for the beginning several cycles and (d) rGESP at different current densities in 1 M H_2SO_4.

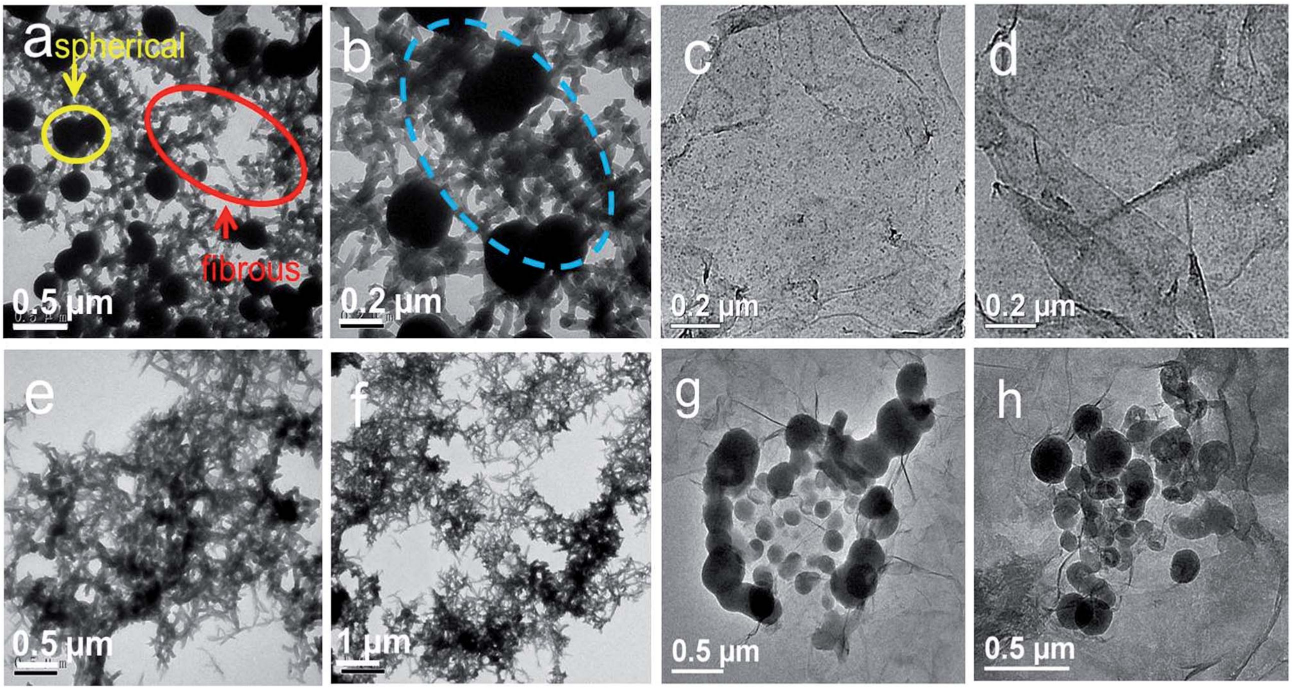

Fig. 10 TEM images of (a and b) rGEPS and (c and d) rGES. TEM images of PANI prepared in (e and f) ethanol and (g and h) PANI.

direct contact between spherical and fibrous PANI, and thus, weakens the excessive winding tendency between them.

In order to verify the proposed speculations and further reveal the morphology formation conditions of rGESP, we prepared rGESP in pure ethanol and water. Fig. 10c and d are the images of rGES-10 wt% for comparison. Fig. 10e, f, g and h show the morphology of rGESP prepared in pure ethanol and water, respectively. For comparison, one can see that PANI mainly exhibits a fibrous character (Fig. 10e and f) when prepared in pure ethanol and shows a spherical shape in rGESP when fabricated in pure water (Fig. 10g and h). A small amount of lamellar rGE is inlaid in fibrous or spherical PANI structures. The observations are consistent with proposed speculations.

The improved specific capacitance of rGESP may be partly attributed to the morphology changes and the synergy of materials. In particular, multiple dimensions including 0D, 1D and 2D of materials simultaneously exist in the rGESP matrix. The assembly of these multiple dimensions produces great quantities of contact gaps, forming porous structures, including micro and nano open-channels. The special porous architecture can not only make full use of the high specific area of rGE, SiO_2 and PANI nanoparticles, but also can provide abundant ion transfer paths, increasing the specific capacitance of rGESP.

Fig. 11a shows the Nyquist plots of rGE, rGES, PANI and rGESP tested in 1 M H_2SO_4 to further assess the effect of rGES on the capacitive energy storage of PANI. The high frequency intercepts of the real axis give the magnitude of the electrolyte resistance (R_s),[51] and the solution resistances for the three electrodes are almost the same. The diameter of the semicircle in the high frequency region gives an indication of charge transfer resistance (R_{ct}).[52,53] Compared with PANI, rGE, rGES and rGESP show smaller diameters, which indicate smaller electron transfer resistance. At low frequency, the line of rGESP is more perpendicular to the real axis than those of rGE, rGES and PANI, indicating a better capacitive behavior,[54] which is consistent with the outcomes of the CV tests. These improvements may be due to the synergistic effects of rGES and PANI, leading to a better capacitive performance for supercapacitors. Moreover, the integration of nanoscale SiO_2 also increases the ion accessibility on the electrode surface by forming voids between rGE and PANI.

Furthermore, rGESP shows improved cycling stability, retaining 91% of the initial performance after 1500 charge/discharge cycles (Fig. 11b). It is much higher than that of PANI (11%, 500 cycles) and rGEP (79%). The rapid decline of PANI in cycling performance can be ascribed to the cross aggregation of PANI chains during repeated swelling/shrinkage (doping/de-doping) in the cycling process. Despite the contraction and expansion that still exists in rGESP, the cross agglomeration of PANI caused by swelling/shrinkage is suppressed greatly by rGES. Moreover, the integration of SiO_2 helps to increase the ion accessibility on the electrode surface by forming voids between rGE and PANI. Thus, rGES is demonstrated to be able to improve the cycling life of PANI based supercapacitors.

The energy density and power density of the electrode materials can be calculated by eqn (2) and (3).[55,56]

$$E = \frac{1}{2} C_s V^2 \tag{2}$$

$$P = \frac{E}{t} \tag{3}$$

where V is the voltage drop upon discharge, and t is the discharging time. Ragone plots of rGE, rGES, PANI, rGEP and rGESP electrode materials for half cells are presented in Fig. 11c. Compared with rGE, rGES, PANI and rGEP, rGESP is more suitable as a supercapacitor material as it has a higher energy and power density. Its energy density is estimated to be 28.1 W h kg^{-1} at a power density of 721.4 W kg^{-1},[57] which is competitive to the reported graphene/metal (oxide)/polymers.[58] Compared with rGESP, the energy densities of rGE, rGES, PANI and rGEP are only 6.8, 11.8, 24.9 and 27.5 W h kg^{-1}, while the power densities are 113.1, 304.5, 642.6 and 667 W kg^{-1}, respectively, calculated at 5 mV s^{-1}. Remarkably, the results indicate that suitable SiO_2 modification for rGE has resulted in better application potential than rGE in PANI based energy storage.

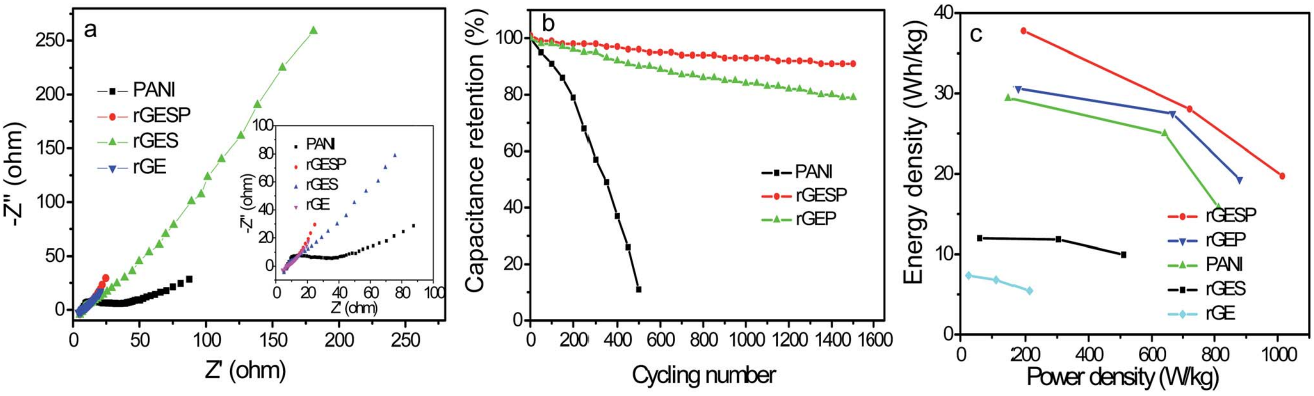

Fig. 11 (a) EIS of rGE, rGES, PANI and rGESP. (b) The C_s retention proportion of rGEP, PANI and rGESP (0.5 wt% SiO_2) at 0.1 A g^{-1} during 1500 cycles, (c) Ragone plots of rGE, rGES, PANI, rGEP and rGESP electrodes. All data were obtained in 1 mol L^{-1} H_2SO_4.

4. Conclusions

Microstructure designable rGES were prepared and demonstrated to be a multifunctional material with potential applications in silicone enhancement and polyaniline based supercapacitors. Generally, the relative content of SiO_2 and rGE largely impacts the microstructure of rGES and further determines the final functions. On the one hand, lamellar rGES shows a positive impact on the polyaniline supercapacitors with longer cycling life due to better structural stability. On the other hand, sandwich-like rGES mainly acts as a favorable reinforcing filler for silicone matrixes, exhibiting improved mechanical strength for the rGE due to better compatibility and dispersion. Moreover, 3D dendritic rGES plays the role of a demarcation point, exhibiting both electrical storage and mechanical enhancing properties, though not the best point. Based on these, one can easily obtain the required functions by regulating the microstructure of rGES and the preparation conditions of the corresponding polymer matrixes.

Acknowledgements

This work was supported by the National Natural Science Foundation of China (No. 21303036, 51303069, 21576138 and 51572125), Zhejiang Provincial Natural Science Foundation of China (LQ13B040002, LY14E030010), Start-up Fund of Hangzhou Normal University (2012QDL021), the Fundamental Research Funds for the Central Universities of China (No. 30920130111003 and 30920140122003), Program for NCET-12-0629, the Ph. D. Programs Foundation of Ministry of Education of China (No. 20133219110018), Qing Lan Project and Six Major Talent Summit (XNY-011), the Science and Technology Support Plan (No. BE2013126), and PAPD of Jiangsu Province, China.

Notes and references

1 N. Behabtu, C. C. Young, D. E. Tsentalovich, O. Kleinerman, X. Wang, A. W. K. Ma, E. A. Bengio, R. F. ter Waarbeek, J. J. de Jong, R. E. Hoogerwerf, S. B. Fairchild, J. B. Ferguson, B. Maruyama, J. Kono, Y. Talmon, Y. Cohen, M. J. Otto and M. Pasquali, *Science*, 2013, **339**, 182–186.

2 K. Evanoff, J. Benson, M. Schauer, I. Kovalenko, D. Lashmore, W. J. Ready and G. Yushin, *ACS Nano*, 2012, **6**, 9837–9845.

3 R. F. Gibson, *Compos. Struct.*, 2010, **92**, 2793–2810.

4 Z. F. Jiang, D. L. Jiang, Z. X. Yan, D. Liu, K. Qian and J. M. Xie, *Appl. Catal., B*, 2015, **170**, 195–205.

5 V. L. Reena, C. Pavithran, V. Verma and J. D. Sudha, *J. Phys. Chem. B*, 2010, **114**, 2578–2585.

6 L. L. Chen, Y. Liu, Y. Zhao, N. Chen and L. T. Qu, *Nanotechnology*, 2016, 27.

7 K. H. S. Iessa, Y. Zhang, G. A. Zhang, F. Xiao and S. Wang, *J. Power Sources*, 2016, **302**, 92–97.

8 X. Hu, M. Tian, L. Qu, S. Zhu and G. Han, *Carbon*, 2015, **95**, 625–633.

9 C.-L. Huang, C.-C. Huang, F.-D. Mai, C.-L. Yen, S.-H. Tzing, H.-T. Hsieh, Y.-C. Ling and J.-Y. Chang, *J. Mater. Chem. B*, 2015, **3**, 651–664.

10 L. Huang, Z. Zhang, Z. Li, B. Chen, X. Ma, L. Dong and L.-M. Peng, *ACS Appl. Mater. Interfaces*, 2015, **7**, 9581–9588.

11 S. Jang, E. Hwang, Y. Lee, S. Lee and J. H. Cho, *Nano Lett.*, 2015, **15**, 2542–2547.

12 P. Bhattacharya, S. Dhibar, G. Hatui, A. Mandal, T. Das and C. K. Das, *RSC Adv.*, 2014, **4**, 17039–17053.

13 A. Bhirud, S. Sathaye, R. Waichal, C.-J. Park and B. Kale, *J. Mater. Chem. A*, 2015, **3**, 17050–17063.

14 A. Du, Z. Zhu and S. C. Smith, *J. Am. Chem. Soc.*, 2010, **132**, 2876–2877.

15 Y. Fu, Q. Chen, M. He, Y. Wan, X. Sun, H. Xia and X. Wang, *Ind. Eng. Chem. Res.*, 2012, **51**, 11700–11709.

16 N. Youngblood, Y. Anugrah, R. Ma, S. J. Koester and M. Li, *Nano Lett.*, 2014, **14**, 2741–2746.

17 J. Yan, Y. Ding, C. Hu, H. Cheng, N. Chen, Z. Feng, Z. Zhang and L. Qu, *J. Mater. Chem. A*, 2014, **2**, 16786–16792.

18 X. Zhang, D. Liu, L. Yang, L. Zhou and T. You, *J. Mater. Chem. A*, 2015, **3**, 10031–10037.

19 Z. Zhang, Y. Dong, F. Xiao and S. Wang, *RSC Adv.*, 2015, **5**, 83480–83485.

20 D. Yu, L. Wei, W. Jiang, H. Wang, B. Sun, Q. Zhang, K. Goh, R. Si and Y. Chen, *Nanoscale*, 2013, **5**, 3457–3464.

21 M. Yusuf, F. M. Elfghi, S. A. Zaidi, E. C. Abdullah and M. A. Khan, *RSC Adv.*, 2015, **5**, 50392–50420.

22 X. Yao, W. Yu, X. Xu, F. Chen and Q. Fu, *Nanoscale*, 2015, **7**, 3959–3964.

23 C. Wang, X. He, Y. Shang, Q. Peng, Y. Qin, E. Shi, Y. Yang, S. Wu, W. Xu, S. Du, A. Cao and Y. Li, *J. Mater. Chem. A*, 2014, **2**, 14994–15000.

24 T.-N. Ye, W.-J. Feng, B. Zhang, M. Xu, L.-B. Lv, J. Su, X. Wei, K.-X. Wang, X.-H. Li and J.-S. Chen, *J. Mater. Chem. A*, 2015, **3**, 13926–13932.

25 Q. L. Hao, H. L. Wang, X. J. Yang, L. D. Lu and X. Wang, *Nano Res.*, 2011, **4**, 323–333.

26 H. L. Wang, Q. L. Hao, X. J. Yang, L. D. Lu and X. Wang, *Electrochem. Commun.*, 2009, **11**, 1158–1161.

27 H. L. Wang, Q. L. Hao, X. J. Yang, L. D. Lu and X. Wang, *ACS Appl. Mater. Interfaces*, 2010, **2**, 821–828.

28 H. L. Wang, Q. L. Hao, X. J. Yang, L. D. Lu and X. Wang, *Nanoscale*, 2010, **2**, 2164–2170.

29 X. F. Xia, Q. L. Hao, W. Lei, W. J. Wang, H. L. Wang and X. Wang, *J. Mater. Chem.*, 2012, **22**, 8314–8320.

30 S. Wu, R. B. Ladani, J. Zhang, E. Bafekrpour, K. Ghorbani, A. P. Mouritz, A. J. Kinloch and C. H. Wang, *Carbon*, 2015, **94**, 607–618.

31 Y. Xue, Y. Liu, F. Lu, J. Qu, H. Chen and L. Dai, *J. Phys. Chem. Lett.*, 2012, **3**, 1607–1612.

32 L. Yang, S. L. Phua, C. L. Toh, L. Zhang, H. Ling, M. Chang, D. Zhou, Y. Dong and X. Lu, *RSC Adv.*, 2013, **3**, 6377–6385.

33 Y.-K. Yang, C.-E. He, R.-G. Peng, A. Baji, X.-S. Du, Y.-L. Huang, X.-L. Xie and Y.-W. Mai, *J. Mater. Chem.*, 2012, **22**, 5666–5675.

34 L.-F. Zhang and C.-Y. Zhang, *Nanoscale*, 2014, **6**, 1782–1789.

35 M. Zhang, R. Li, X. Chang, C. Xue and X. Gou, *J. Power Sources*, 2015, **290**, 25–34.

36 Z. Zhang, F. Xiao, Y. Guo, S. Wang and Y. Liu, *ACS Appl. Mater. Interfaces*, 2013, **5**, 2227–2233.

37 B. Zhao, Y. Zheng, F. Ye, X. Deng, X. Xu, M. Liu and Z. Shao, *ACS Appl. Mater. Interfaces*, 2015, **7**, 14446–14455.

38 R. Kumar, J.-H. Oh, H.-J. Kim, J.-H. Jung, C.-H. Jung, W. G. Hong, H.-J. Kim, J.-Y. Park and I.-K. Oh, *ACS Nano*, 2015, **9**, 7343–7351.

39 S. Liu, Y. Dong, C. Zhao, Z. Zhao, C. Yu, Z. Wang and J. Qiu, *Nano Energy*, 2015, **12**, 578–587.

40 R. K. Upadhyay, N. Soin and S. S. Roy, *RSC Adv.*, 2014, **4**, 3823–3851.

41 G. Wang, G. Chen, Z. Wei, X. Dong and M. Qi, *Mater. Chem. Phys.*, 2013, **141**, 997–1004.

42 K. Yao, J. Gong, N. Tian, Y. Lin, X. Wen, Z. Jiang, H. Na and T. Tang, *RSC Adv.*, 2015, **5**, 31910–31919.

43 W. Ye, L. Zhang and C. Li, *RSC Adv.*, 2015, **5**, 25450–25456.

44 J. Chen, Y. R. Li, L. Huang, C. Li and G. Q. Shi, *Carbon*, 2015, **81**, 826–834.

45 X. L. Wang and W. Q. Dou, *Thermochim. Acta*, 2012, **529**, 25–28.

46 R. Gusain, H. P. Mungse, N. Kumar, T. R. Ravindran, R. Pandian, H. Sugimura and O. P. Khatri, *J. Mater. Chem. A*, 2016, **4**, 926–937.

47 H. V. Kumar, S. J. Woltornist and D. H. Adamson, *Carbon*, 2016, **98**, 491–495.

48 W. L. Xie and L. B. Hu, *Food Chem.*, 2016, **197**, 92–99.

49 N. Parveen, M. O. Ansari and M. H. Chot, *Ind. Eng. Chem. Res.*, 2016, **55**, 116–124.

50 J. J. Liu, Y. F. Deng, X. H. Li and L. F. Wang, *ACS Sustainable Chem. Eng.*, 2016, **4**, 177–187.

51 W. Wang, Q. Hao, W. Lei, X. Xia and X. Wang, *J. Power Sources*, 2014, **269**, 250–259.

52 W. B. Fu, Y. L. Wang, W. H. Han, Z. M. Zhang, H. M. Zha and E. Q. Xie, *J. Mater. Chem. A*, 2016, **4**, 173–182.

53 Y. S. Fu, Q. Chen, M. Y. He, Y. H. Wan, X. Q. Sun, H. Xia and X. Wang, *Ind. Eng. Chem. Res.*, 2012, **51**, 11700–11709.

54 W. Q. Zhao, S. S. Wang, C. H. Wang, S. T. Wu, W. J. Xu, M. C. Zou, A. Ouyang, A. Y. Cao and Y. B. Li, *Nanoscale*, 2016, **8**, 626–633.

55 Q. Y. Lv, S. Wang, H. Y. Sun, J. Luo, J. Xiao, J. W. Xiao, F. Xiao and S. Wang, *Nano Lett.*, 2016, **16**, 40–47.

56 Q. Hao, X. Xia, W. Lei, W. Wang and J. Qiu, *Carbon*, 2015, **81**, 552–563.

57 Z. H. Zhao, G. F. Richardson, Q. S. Meng, S. M. Zhu, H. C. Kuan and J. Ma, *Nanotechnology*, 2016, 27.

58 X. Xia, W. Lei, Q. Hao, W. Wang and X. Wang, *Electrochim. Acta*, 2013, **99**, 253–261.